



## OPEN ACCESS

## EDITED BY

Yuanjia Han,  
China University of Geosciences, China

## REVIEWED BY

Sherif Farouk,  
Egyptian Petroleum Research Institute, Egypt  
Oluwasanmi Olabode,  
Covenant University, Nigeria  
Binyu Wang,  
China University of Petroleum, Beijing, China

## \*CORRESPONDENCE

Qiuyue Zhang,  
✉ zqy13653124701@163.com

RECEIVED 23 October 2025

REVISED 23 December 2025

ACCEPTED 29 December 2025

PUBLISHED 14 January 2026

## CITATION

Shi J, Zhang Q, Liu J, Zhang M, Shi L and Wang D (2026) Microscopic pore-throat utilization characteristics of advanced fracturing-flooding water injection in tight oil reservoirs.

*Front. Earth Sci.* 13:1730752.

doi: 10.3389/feart.2025.1730752

## COPYRIGHT

© 2026 Shi, Zhang, Liu, Zhang, Shi and Wang.

This is an open-access article distributed under the terms of the [Creative Commons Attribution License \(CC BY\)](https://creativecommons.org/licenses/by/4.0/). The use, distribution or reproduction in other forums is permitted, provided the original author(s) and the copyright owner(s) are credited and that the original publication in this journal is cited, in accordance with accepted academic practice. No use, distribution or reproduction is permitted which does not comply with these terms.

# Microscopic pore-throat utilization characteristics of advanced fracturing-flooding water injection in tight oil reservoirs

Jianchao Shi<sup>1</sup>, Qiuyue Zhang<sup>2\*</sup>, Jian Liu<sup>1</sup>, Meng Zhang<sup>2</sup>, Luming Shi<sup>1</sup> and Di Wang<sup>1</sup>

<sup>1</sup>Exploration & Development Research Institute of Petrol China Changqing Oilfield Company, Xi'an, China, <sup>2</sup>College of Petroleum Engineering, China University of Petroleum (Beijing), Beijing, China

Advanced fracturing-flooding water injection (AFWI) technology provides an effective approach to overcoming the limitations of conventional waterflooding in tight oil reservoirs, particularly the issues of low sweep efficiency and poor recovery. Nevertheless, the mechanisms governing pore-throat utilization during this process remain insufficiently understood. In this study, a combination of nuclear magnetic resonance (NMR) experiments and finite element (FE) simulations was employed to investigate the microscopic displacement behavior of tight cores under different scales of advanced fracturing-flooding water injection. The results show that AFWI increased the initial displacement pressure differential from 6.34 MPa (pre-injection volume ( $V_{pre}$ ) = 0) to 7.56 MPa ( $V_{pre}$  = 0.3) and 8.45 MPa ( $V_{pre}$  = 0.6), advanced the waterflood front by 1.5 cm ( $V_{pre}$  = 0.3) and 2.6 cm ( $V_{pre}$  = 0.6), and raised ultimate oil recovery from 35.5% to 40.5% and 43.5%. Low-field nuclear magnetic resonance (LF-NMR) spectra were calibrated to pore radius via mercury intrusion, showing enhanced recovery in medium-small throats under larger  $V_{pre}$ . Microscopic simulations revealed that increasing  $V_{pre}$  intensifies the pressure gradient between injection and production ends, activating flow pathways within smaller pores and improving overall pore-throat utilization. The integrated experimental and numerical findings advance understanding of pore-scale fluid dynamics in tight reservoirs and provide theoretical guidance for optimizing AFWI strategies.

## KEYWORDS

advanced fracturing-flooding water injection, microscopic numerical simulation, microscopic pore-throat utilization characteristics, nuclear magnetic resonance (NMR) experiment, tight oil reservoirs

## 1 Introduction

As the exploration and development of oil and gas resources accelerates, tight oil and gas have gradually emerged as crucial resources supporting the global oil and gas revolution (Yang et al., 2017; Li et al., 2022a; Yan et al., 2024; Jia et al., 2025; Wang et al., 2021). Tight reservoirs are characterized by poor reservoir properties, small pore throats, a significant proportion of small throat openings, and strong microscopic heterogeneity

(Zhang et al., 2016; Song et al., 2020; Shi et al., 2015; Feng et al., 2017; Yang et al., 2022b; Yang et al., 2022a). These characteristics lead to high injection pressures, limited effective connectivity, capillary-dominated flow regimes under typical waterflood conditions, and challenges in the development process, including high water injection pressures and low oil recoveries (Wang et al., 2019; Xue et al., 2025). Waterflooding in tight reservoirs is governed by low-Reynolds-number, capillary-controlled two-phase flow. Key dimensionless groups include the mobility ratio ( $M$ ) and the capillary number. With kerosene and water,  $M < 1$ , indicating a potentially stable displacement in homogeneous media; however, microscopic heterogeneity and capillary end effects restrict the advance of the waterflood front and strand oil in small throats. To address these development challenges, several oil fields have recently proposed advanced fracturing-flooding water injection (Wang et al., 2025; Li et al., 2024; Gao et al., 2024; Zhao et al., 2025; Cao et al., 2024; Oluwasanmi et al., 2021). By implementing water injection at pressures close to the fracture pressure, this method replenishes reservoir energy and creates micro-fractures that expand the swept volume, increase pore throat dimensions, and enhance water flow channels. However, the technology for advanced fracturing-flooding water injection is still in its infancy, and the mechanisms supporting this technique require further refinement. Therefore, it is imperative to clarify the characteristics of pore throat utilization during advanced fracturing-flooding water injection in tight oil reservoirs.

Currently, nuclear magnetic resonance-assisted core displacement experiments provide a rapid, nondestructive means to detect fluid distribution patterns and pore throat utilization characteristics within core samples (Tan et al., 2019; Zhou et al., 2019; Jin et al., 2021; Mahmoud et al., 2020; Chelsea et al., 2020; Krakowska and Puskarczyk 2015). Employing this methodology, numerous researchers have executed core displacement experiments to examine the pore throat utilization characteristics linked to diverse development strategies (Yang et al., 2022b; Sun et al., 2024; Yang et al., 2024; Qi et al., 2024; Lang et al., 2021; Yao et al., 2023). However, research pertaining to nuclear magnetic resonance experiments in the context of advanced fracturing-flooding water injection remains scarce. In exploring the microscopic mechanisms through which advanced fracturing-flooding water injection enhances pore-throat utilization (Zhang et al., 2025; Ren et al., 2025), many researchers have employed techniques such as pore network modeling (Yang et al., 2022a; Lin et al., 2021; Xu et al., 2023), lattice Boltzmann methods (Li et al., 2025; Hou et al., 2021; Wei et al., 2023; Mohnke et al., 2014; Jamal et al., 2022), and interface capture approaches for simulating microscopic pore throats (Feng et al., 2025; Lu et al., 2020). Among these, interface capture methods exemplified by the phase field approach are proficient in handling the dynamics of two-phase interfaces within complex geometrical pore throats, rendering them appropriate for simulating microscopic two-phase flow in intricate pore structures. However, there are still limited studies that concentrate on micro-simulation of pore throats in relation to advanced fracturing-flooding water injection techniques.

To address the existing gap in research concerning the enhancement of pore throat utilization through advanced fracturing-flooding water injection technology, this study employs a combination of nuclear magnetic resonance experiments and

microscopic pore throat simulation techniques. An analysis is conducted on the pressure increment, pore throat utilization characteristics, and underlying microscopic utilization mechanisms associated with different scales of advanced fracturing-flooding water injection technologies.

## 2 Physical experiment

### 2.1 Experimental materials and equipment

The oil sample used in the experiment is anhydrous kerosene, exhibiting a density of  $0.8 \text{ g/cm}^3$  and a viscosity of  $2.5 \text{ mPa s}$  at  $25^\circ\text{C}$  and  $0.1 \text{ MPa}$ . The water sample used in the experiment is high-purity deuterium oxide ( $\text{D}_2\text{O}$ ) with a density of  $1.105 \text{ g/cm}^3$  and a viscosity of  $1.095 \text{ mPa s}$  under the same conditions of  $25^\circ\text{C}$  and  $0.1 \text{ MPa}$ . In this experiment, three tight cores from the Y District of the HuaQing Oilfield, located in the Ordos Basin, are used, and the physical properties of the cores are shown in Table 1.

We used anhydrous kerosene as a surrogate for light crude oil for three reasons: (i) reproducibility and safety—kerosene has a stable, well-characterized composition and physical properties, reducing variability due to crude compositional changes and minimizing hazards; (ii) NMR compatibility—kerosene's hydrogen signal is strong and consistent, while deuterium oxide ( $\text{D}_2\text{O}$ ) suppresses water signals, enabling clean separation of oil-phase responses without interference from paramagnetic species occasionally present in crude; (iii) wettability and flow similarity—kerosene closely approximates the behavior of light tight oils under laboratory conditions, allowing us to isolate the effects of pressure gradient and pore-scale geometry on waterflooding performance. Accordingly, we refer to the oil phase as “kerosene” throughout the manuscript, and all NMR and simulation analyses are based on kerosene–water systems.

The experimental setup comprises three primary components: the core displacement device, the nuclear magnetic resonance monitoring system, and the metering apparatus. Figure 1 illustrates the configuration of the experimental device. The displacement system consists of an ISCO constant-speed, constant-pressure pump and an intermediate container. The core experimental equipment features a self-developed online nuclear magnetic resonance monitoring system, which includes a low-field nuclear magnetic resonance device (Macro12-150H-I, Suzhou Niumai), a core holder, and a constant-pressure circulating control pump. In this experiment, the Q-CPMG sequence was employed to collect the core throat signals, operating at a resonance frequency of  $12.79 \text{ MHz}$  with a coil diameter of  $25 \text{ mm}$ . The echo time (TE) was set to  $0.5 \text{ ms}$ , with a waiting time of  $6 \text{ s}$  and a total of  $1024$  echoes recorded. Additionally, the HSE sequence was utilized to scan the nuclear magnetic resonance imaging signals. During the experimental process, data measurement occurs through two means: one involves the metering system, which records the pressures at the inlet and outlet ends of the core and the flow rate at the outlet, while the other employs the nuclear magnetic resonance monitoring system to observe the distribution patterns of oil and water throughout the experiment.

TABLE 1 Basic parameters of experimental core.

Core sample	Diameter, cm	Length of core, cm	Porosity, %	Permeability, mD
1	2.56	8.05	9.32	0.24
2	2.46	8.01	11.56	0.25
3	2.53	8.03	12.27	0.24

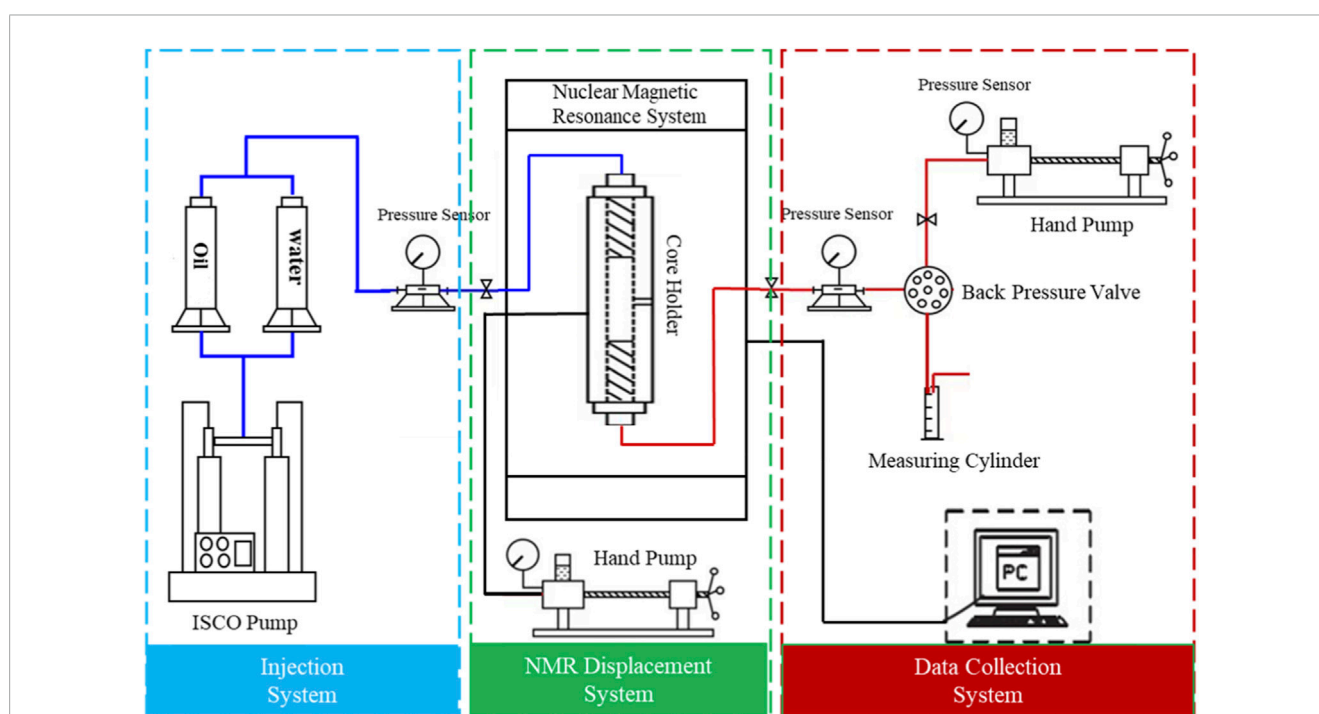


FIGURE 1

Schematic and photograph of the core displacement setup integrated with low-field NMR, including injection system, NMR displacement system, and data collection system.

## 2.2 Experimental design and process

To compare the effects of varying scales of advanced fracturing-flooding water injection, three experimental sets were designed, simulating both conventional water flooding and advanced fracturing-flooding water injection. The first set of conventional water flooding experiments involved a total injection volume of 3 PV (pore volumes). For the second set of advanced fracturing-flooding water injection experiments, the total volume injected was also 3 PV, with the pre-injection volumes (the pre-injection volume when production is terminated and the injection pressure approaches the fracture initiation pressure.) set at 0.3 PV and 0.6 PV, corresponding to multiplicative factors in the near-wellbore region. The experimental design details are summarized in Table 2. The experimental steps are as follows:

1. Basic preparations: The materials for the experiment, such as the oil sample, water sample, core, etc., are prepared in accordance with the experimental designs,

and the central device is connected and its airtightness is verified.

2. Core vacuum saturation: The core is placed within the chamber of the vacuum saturation apparatus, where a predetermined negative pressure is established and maintained for a duration of 24 h. This step is designed to expel any gases contained within the core, thereby preparing it for subsequent saturation operations.
3. Formation of bound water and saturation with simulated oil: Initially, the pressure valve of the vacuum saturation apparatus is opened, followed by the injection of water, with the saturation pressure set at 15 MPa for a duration of 7 days. Due to the existing negative pressure within the core, water is able to permeate through the pore spaces. Given the core's dense nature, to achieve thorough saturation, the core is subsequently placed in a holder for water injection and displacement saturation. Following this, oil is used to displace the water, completely expelling all movable water and forming bound water, thereby achieving a fully saturated oil state in the core.

TABLE 2 Experimental scheme.

Core experiment	Water injection method	Pre-injection volume, PV
1	Conventional injection	0
2	Advanced injection	0.3
3	Advanced injection	0.6

During the saturation process, the volumes of the oil and water phases within the core are calculated based on the volumes injected and produced.

- Experimental procedures and data analysis:
  - Synchronous Water Injection via Conventional Core Displacement Experiment: The cylindrical core is configured with the left end serving as the injection side and the right end as the production side. The confining pressure is set at 15 MPa, with a back pressure of 12 MPa. Water is injected at a constant rate of 0.05 mL/min while simultaneously opening the production side. Key parameters such as core displacement pressure differentials, cumulative injection volumes, and the quantities of oil and water produced at the outlet are meticulously recorded.
  - Advanced fracturing-flooding water injection Experiment: This phase is divided into two distinct stages. The first stage involves the advanced fracturing-flooding water injection phase; the production side is closed while water is injected at a constant rate of 0.05 mL/min until a predetermined pore volume (PV) is achieved, at which point the injection phase concludes. The second stage is the continuous water drive phase: the production side is opened, and water injection continues at the same rate of 0.05 mL/min. During this stage, continuous recording of the core displacement pressure differentials, cumulative injection volumes, and oil and water production rates at the outlet is maintained. Throughout each experimental setup, synchronized nuclear magnetic resonance (NMR) imaging is conducted. The experiment concludes when the water cut at the production outlet exceeds 95% or when no additional oil is produced.

## 2.3 NMR monitoring imaging processing method

Under the influence of a static magnetic field and an externally applied low magnetic field, the hydrogen nuclei in the pore throats of kerosene (oil phase) resonate (Yuan et al., 2023; Liu et al., 2022). During the relaxation process, radiofrequency signals are emitted. By receiving these signals and conducting mathematical inversion, we can generate an amplitude-relaxation time curve. The expression of relaxation time is shown in Equation 1 (Li et al., 2022b):

$$\frac{1}{T_2} = \frac{1}{T_{2B}} + \frac{1}{T_{2S}} + \frac{1}{T_{2D}} \quad (1)$$

Where  $T_2$  is the total relaxation time, ms;  $T_{2B}$  is the transverse relaxation time of the filling fluid, ms;  $T_{2S}$  is the

surface transverse relaxation time, ms;  $T_{2D}$  is the transverse relaxation time caused by fluid diffusion in the magnetic field gradient, ms.

Due to the significant interaction between fluids and the surface of the rock within dense cores, the bulk relaxation time ( $T_{2B}$ ) is considerably greater than the relaxation time ( $T_2$ ). Additionally, because the echo time ( $T_E$ ) is relatively small, the diffusion relaxation time ( $T_{2D}$ ) also greatly exceeds  $T_2$ . Consequently, these two terms can be disregarded, allowing the relaxation time to be expressed as follows (Equations 2–4):

$$T_2 = T_{2S} = \frac{1}{\rho\delta} r = Cr \quad (2)$$

$$\delta = \frac{S}{V} r \quad (3)$$

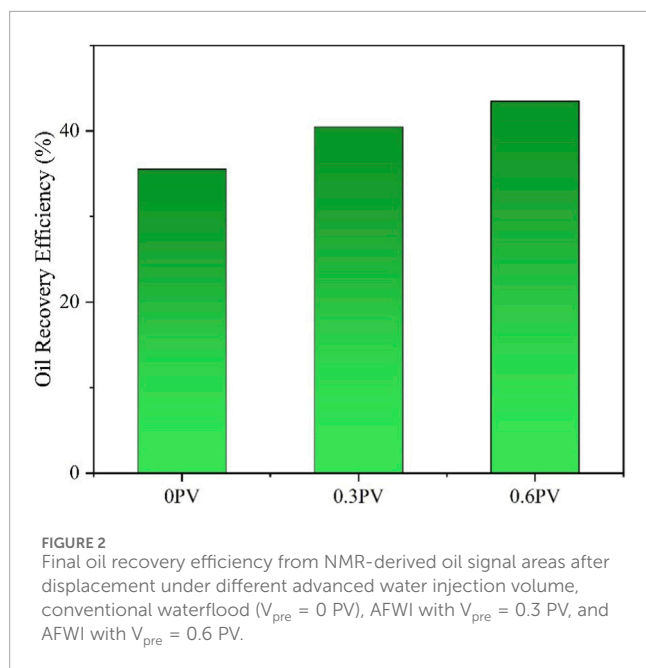
$$C = \frac{1}{\rho\delta} \quad (4)$$

Where  $\rho$  is the relaxation strength constant of the rock surface;  $\delta$  is the pore shape factor;  $S$  is the surface area of rock particles,  $\text{cm}^2$ ;  $V$  is the pore volume,  $\text{cm}^3$ ;  $r$  is the average pore radius, cm;  $C$  is the conversion coefficient,  $\mu\text{m}/\text{ms}$ .

From Equation 2, it is evident that the relaxation time ( $T_2$ ) is directly proportional to the pore radius of the rock, meaning that larger pores correspond to longer relaxation times, while smaller pores are associated with shorter relaxation times. After obtaining the conversion factor ( $C$ ), the  $T_2$  spectrum's horizontal axis can be translated into pore radius, thereby allowing the  $T_2$  spectrum to effectively reflect the distribution of pore sizes within tight sandstone reservoirs.

By calibrating the  $T_2$  curve obtained from NMR scanning of the saturated core with mercury intrusion experiments, we can derive the pore size conversion factor ( $C$ ), enabling the translation of the relaxation time on the original  $T_2$  spectrum into pore throat radius. Following the approach proposed by Li et al., we accumulate the intensity of hydrogen signals from kerosene (oil phase) to generate a cumulative distribution map of the hydrogen signal strength in the core. Based on the  $T_2$  spectrum of the core used in the experiments, pore throats are categorized into three distinct groups: small pore throats ( $0.01 \mu\text{m} < r < 0.1 \mu\text{m}$ ), medium pore throats ( $0.1 \mu\text{m} < r < 0.5 \mu\text{m}$ ), and large pore throats ( $r > 0.5 \mu\text{m}$ ).

During the experimental process, the simulated water used for saturation was a composite deuterium oxide, and the NMR monitoring system was only capable of detecting the hydrogen signal from kerosene (oil phase). Consequently, the nuclear magnetic resonance signals obtained throughout the displacement experiment solely reflect changes in the oil.



The formula for calculating oil recovery efficiency is shown in Equation 5:

$$E = \frac{A_0 - A_1}{A_0} \times 100\% \quad (5)$$

Where  $E$  is the oil recovery efficiency, %;  $A_0$  is the area enclosed by the  $T_2$  spectrum and the horizontal axis over a specific pore radius range after saturation,  $\text{cm}^2$ ;  $A_1$  is the area enclosed by the  $T_2$  spectrum and the horizontal axis over a specific pore radius range after displacement,  $\text{cm}^2$ .

## 2.4 Experimental results analysis

A comparison of the results of three groups of different-scale advanced fracturing-flooding water injection experiments shows that the initial displacement pressure differentials at the onset of waterflooding were recorded as 6.34 MPa, 7.56 MPa, and 8.45 MPa, respectively. This indicates that the advanced fracturing-flooding water injection significantly enhances the displacement pressure differential compared to conventional water injection. As the injection scale increases, the pressure gradient becomes greater, thereby facilitating the establishment of an effective displacement pressure system between the oil and water wells.

Figure 2 depicts the final oil recovery efficiencies after the displacement was completed in the three experimental groups. The ultimate oil recovery efficiencies for the three experiments were recorded at 35.5%, 40.5%, and 43.5%, respectively. These results demonstrate that, compared to conventional water injection, AFWI enhances oil recovery efficiency by 5%. Furthermore, increasing the scale of AFWI further augments the oil recovery efficiency.

The comparative results of the kerosene (oil phase) signal intensity along the core at the conclusion of the advanced

fracturing-flooding water injection experiment are illustrated in Figure 3. This method enables the utilization of the oil phase at the injection end of the core. For the 0.3 PV advanced fracturing-flooding water injection, the advancement distance of the waterflood front was measured at 1.5 cm, while for the 0.6 PV advanced fracturing-flooding water injection, the advancement distance reached 2.6 cm. As the scale of the advanced fracturing-flooding water injection increases, the extent of utilization at the injection end of the core also intensifies, resulting in an expanded advancement distance of the waterflood front.

The comparative results of the kerosene (oil phase) signal intensity along the core at the conclusion of the waterflood displacement following the advanced fracturing-flooding water injection are illustrated in Figure 4. During the pre-injection phase, a certain displacement pressure differential and pressure gradient were established, allowing the fluid within the core to be “activated in advance.” The subsequent continuous water injection further established the displacement pressure differential, facilitating the extraction of this prematurely mobilized fluid. Upon the completion of the displacement, advanced fracturing-flooding water injection exhibited a superior ability to utilize the throat of the core at the injection end. Overall, advanced fracturing-flooding water injection demonstrates a greater extent of utilization compared to synchronous water injection; consequently, increasing the scale of advanced fracturing-flooding water injection can further enhance the utilization of the oil phase within the core.

Nuclear magnetic resonance (NMR) scans of the core were conducted after initial saturation, at the conclusion of synchronous water displacement, and after advanced fracturing-flooding water injection of 0.3 PV and 0.6 PV, yielding the corresponding  $T_2$  spectra. These spectra were then transformed into probability distribution curves of the oil phase within pores of varying radii, as depicted in Figure 5. Upon completion of the displacement, the hydrogen signal intensity of kerosene (oil phase) in the small pore throats experienced a modest decline, while the signal intensity in the large pore throats exhibited a significant reduction. Moreover, as the volume of advanced fracturing-flooding water injection increased, the utilization extent within the core correspondingly intensified. Based on the  $T_2$  spectra from the experimental cores, pore throat radii were categorized as small, medium and large.

Figure 6 illustrates the extent to which different pore throats in the core are mobilized after the completion of displacement following advanced fracturing-flooding water injection. Synchronous water injection primarily mobilizes large pore throats along with a portion of small pore throats. In contrast, advanced fracturing-flooding water injection not only primarily mobilizes large pore throats but also enhances the utilization extent of small pore throats. Both 0.3 PV and 0.6 PV g advanced fracturing-flooding water injection effectively mobilize pore throats of various sizes, predominantly focusing on large throats. However, as the volume of advanced fracturing-flooding water injection increases, the utilization extent of small pore throats also rises. This phenomenon is largely attributed to the fact that a greater volume of advanced fracturing-flooding water injection generates an increased displacement pressure differential and pressure gradient, thereby facilitating the further utilization of the oil phase within the small pore throats.

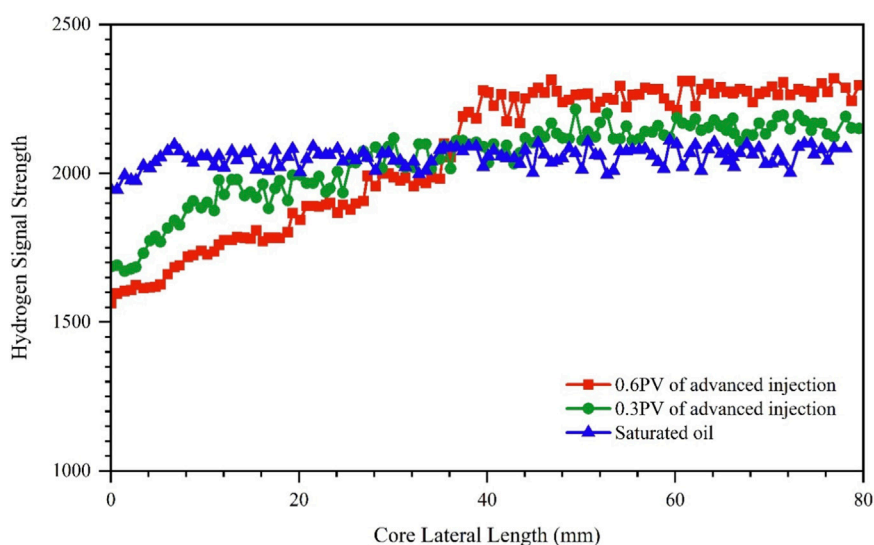


FIGURE 3  
Comparison of kerosene (oil phase) signal intensity along the core at the end of pre-injection.

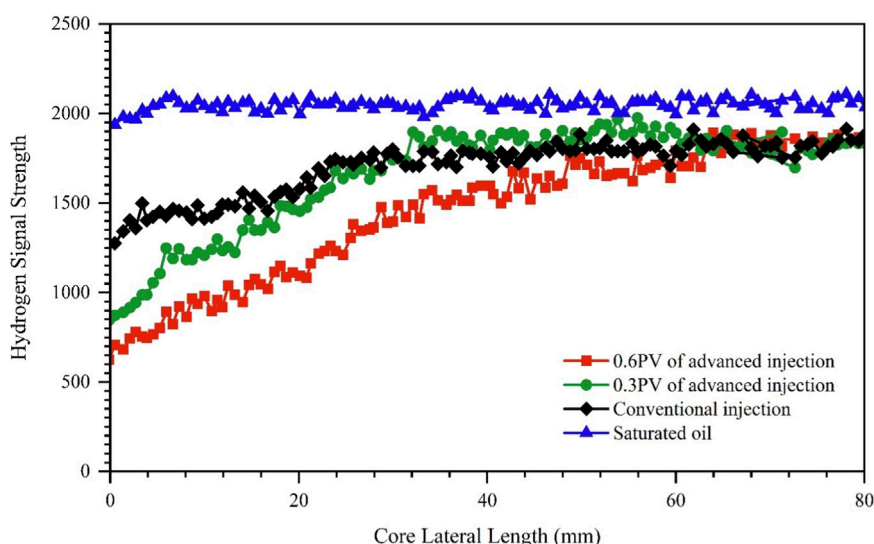


FIGURE 4  
Comparison of kerosene (oil phase) signal intensity along the core at the end of displacement.

### 3 Pore-scale numerical simulation

A comparative analysis between traditional water injection experiments and advanced fracturing-flooding water injection core experiments revealed that the advanced fracturing-flooding water injection elevated the pressure at the inlet section of the core. This phenomenon elucidated the mechanism by which advanced fracturing-flooding water injection enhances oil recovery efficiency and the characteristics of pore throat utilization at the core scale. This section will utilize the commercial simulation software COMSOL Multiphysics to conduct micro-simulations at the pore throat scale, further elaborating on the characteristics of pore throat utilization in

advanced fracturing-flooding water injection for tight oil reservoirs from a microscopic perspective.

#### 3.1 Model establishment and assumptions

The model underwent a binarization process through threshold segmentation of the scanned image of the cast specimen (Figure 7a), followed by the application of MATLAB code to smooth the boundaries and eliminate noise, resulting in the pore throat structure distribution portrayed in Figure 7b. The model dimensions were  $30\ \mu\text{m} \times 30\ \mu\text{m}$ . Subsequently, the obtained point-line formatted image was imported into COMSOL software,

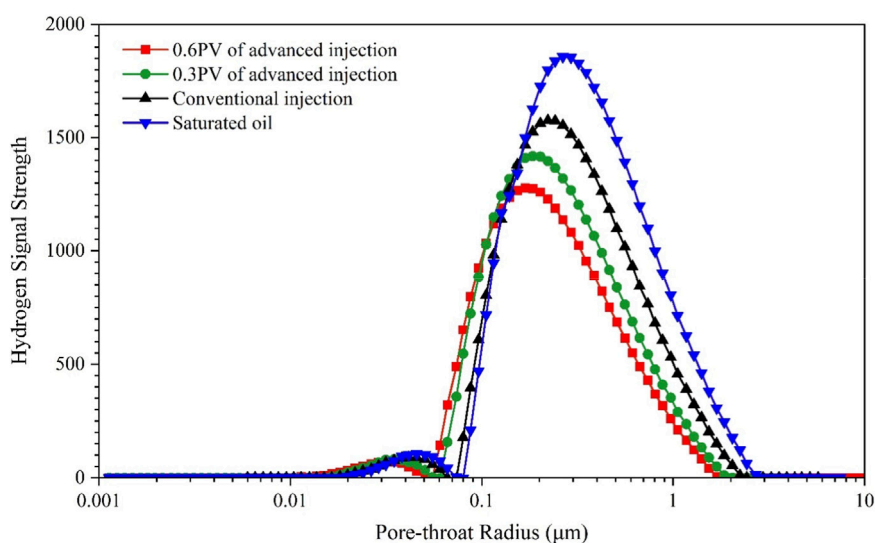


FIGURE 5  
Distribution curves of oil phase in pores with different radii at the end of displacement.

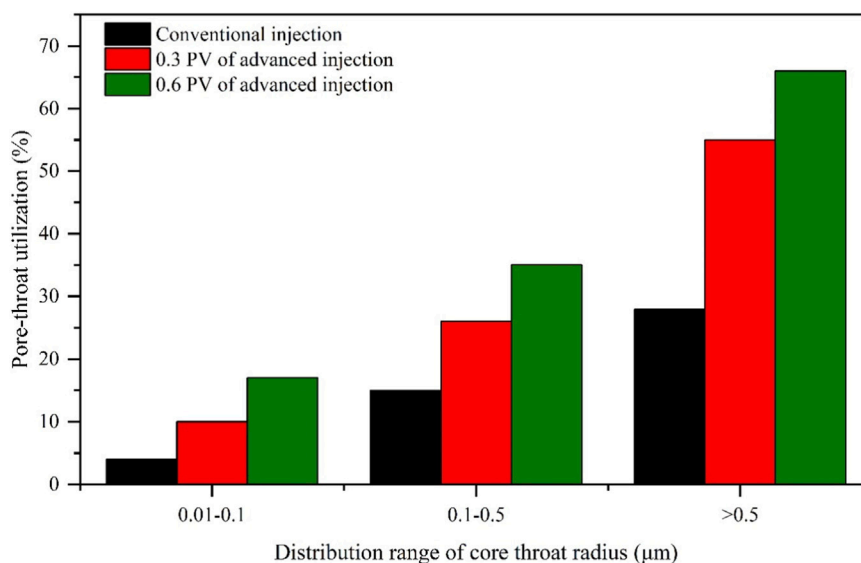


FIGURE 6  
Different pore throat producing degree of core at the end of displacement after pre-injection.

where the geometric model was subjected to mesh partitioning using Delaunay's free triangular meshing, yielding the model displayed in Figure 7c with a total of 105,624 elements and a minimum element mass of 0.1169. The initial fluid distribution within the model is depicted in Figure 7d, where blue represents the aqueous phase and red represents the oil phase. The simulation parameters of the model are shown in Table 3.

The pore-scale numerical model is based on the following assumptions.

- The whole simulation process encompasses solely the two phases of oil and water.

- Both the oil and water phases are regarded as incompressible fluids.
- The system is maintained under isothermal conditions, with no temperature changes resulting from the injection of water.
- The flow process is a two-dimensional horizontal flow, ignoring the effect of gravity.

### 3.2 Governing equations

In this simulation, the phase-field method was employed to couple the Cahn-Hilliard equation with the Navier-Stokes equations via surface tension. This approach allows for an accurate description

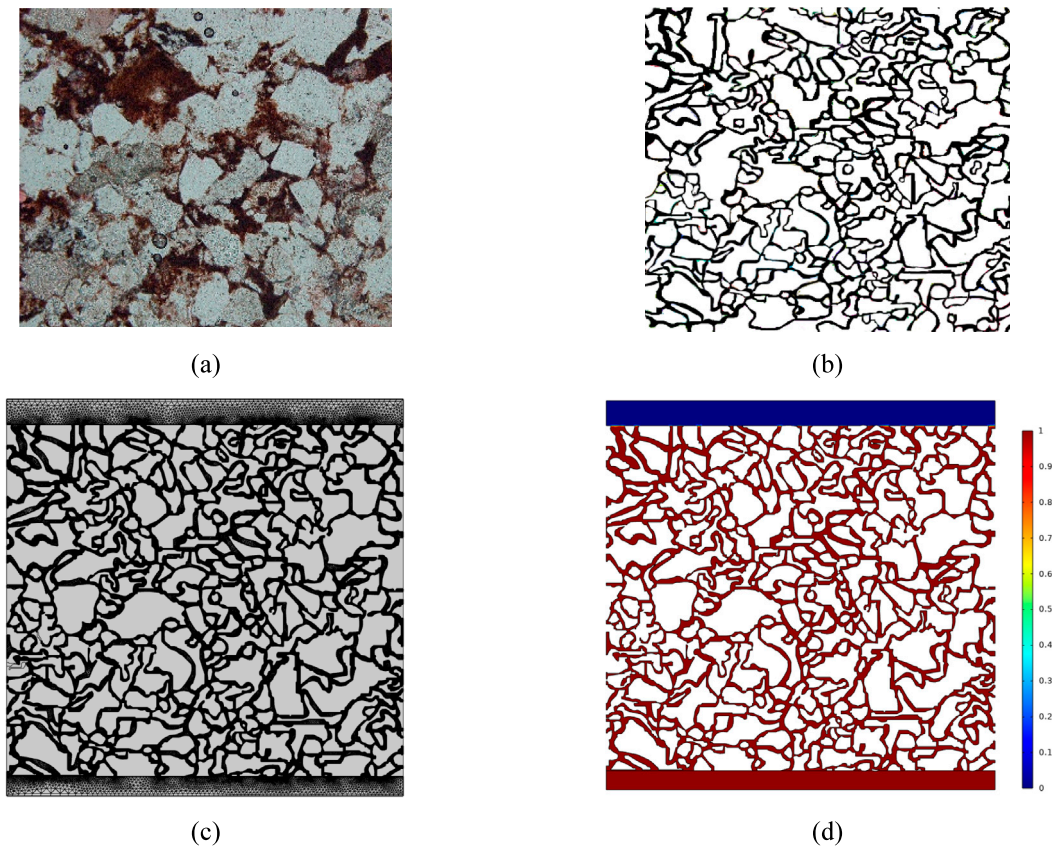


**FIGURE 7** Pore-scale model construction and meshing. (a) SEM image of tight sandstone. (b) Binarized image after thresholding and boundary smoothing. (c) Delaunay free-triangle mesh. (d) Initial oil (red)-water (blue) distribution for CH-NS simulation.

**TABLE 3** Main computational parameters of the model.

Model parameters	Values	Units
Water and oil viscosity	1,2.5	mPa·s
Water and oil density	1,000,850	Kg/m <sup>3</sup>
Oil-water interfacial tension	25	mN/m
Contact angle	60	°
Inlet velocity	100	μm/s
Interface thickness	0.1	μm
Mobility	1	M·s/kg

of the fluid flow processes of two-phase fluids while ensuring mass conservation. The Cahn-Hilliard equation primarily describes the phase separation process, which includes the separation of two-phase or multiphase fluids, expressed as follows (Equation 6):

$$\begin{cases} \frac{\partial \phi}{\partial t} + u \cdot \nabla \phi = \frac{\gamma \lambda}{\epsilon^2} \Delta \psi \\ \psi = -\epsilon^2 \Delta \phi + \phi(\phi^2 - 1) \end{cases} \quad (6)$$

Where  $u$  is the fluid flow velocity, m/s;  $\gamma$  is the mobility, m<sup>3</sup>·s/kg;  $\lambda$  is the mixed energy density, N;  $\epsilon$  is the interfacial thickness, m;  $\psi$  is the phase field auxiliary variable;  $\phi$  is the dimensionless phase field variable. In the oil-water two-phase flow,  $\phi = 1$  represents the oil phase, and  $\phi = 0$  represents the water phase. In the oil-water transition region, the phase field variable  $\phi$  varies continuously between 1 and 0. The fluid properties corresponding to the phase-field variable can be expressed as follows (Equation 7):

$$n(\phi) = \frac{1 + \phi}{2} n_1 + \frac{1 - \phi}{2} n_2 \quad (7)$$

Where  $n_1$  and  $n_2$  are the physical properties of the oil and water phases, thereby achieving a smooth transition of fluid properties at the interface.

The Navier-Stokes equations are primarily employed to delineate the variations of mass and momentum in steady-state fluid flow. By incorporating interfacial tension as a body force within the Navier-Stokes equations, it becomes possible to characterize the flow processes of two-phase fluids. The corresponding expression is as follows (Equation 8):

$$\begin{cases} \rho \frac{\partial u}{\partial t} + \rho u \cdot \nabla u = -\nabla p I + \nabla \cdot [\mu(\nabla u + \nabla u^T)] + F_{st} \\ \nabla \cdot u = 0 \end{cases} \quad (8)$$

Where  $\rho$  is the density,  $\text{kg/s}^3$ ;  $p$  is the pressure, Pa;  $I$  is the unit vector;  $\mu$  is the viscosity,  $\text{mPa}\cdot\text{s}$ ;  $F_{st}$  is the interfacial tension force term.

Combined with the Cahn-Hilliard equation, a two-phase Cahn-Hilliard-Navier-Stokes flow system can be obtained as Equation 9.

$$\begin{cases} \frac{\partial \phi}{\partial t} + u \cdot \nabla \phi = \frac{\gamma \lambda}{\varepsilon^2} \Delta \psi \\ \psi = -\varepsilon^2 \Delta \phi + \phi(\phi^2 - 1) \\ \rho \frac{\partial u}{\partial t} + \rho u \cdot \nabla u = -\nabla p I + \nabla \cdot [\mu(\nabla u + \nabla u^T)] + F_{st} \\ \nabla \cdot u = 0 \end{cases} \quad (9)$$

For the surface of rock particles, the boundary conditions considering the contact angle of oil and water are shown in Equations 10–12 (Yue et al., 2006; Zhou et al., 2010):

$$u = 0 \quad (10)$$

$$m \cdot \varepsilon^2 \nabla \phi = \varepsilon^2 \cos(\theta_c) |\nabla \phi| \quad (11)$$

$$m \cdot \frac{\gamma \lambda}{\varepsilon^2} \Delta \psi = 0 \quad (12)$$

Where  $\theta_c$  is the contact angle,  $^\circ$ .

COMSOL Multiphysics is a powerful software tool for multiphysics simulation. This software is used to mesh and solve the finite element problem. The backward difference method is used to discretize time, and the MUMPS direct solver is used to solve the problem. The utilization characteristics of pore throats during advanced fracturing-flooding water injection at various scales are simulated.

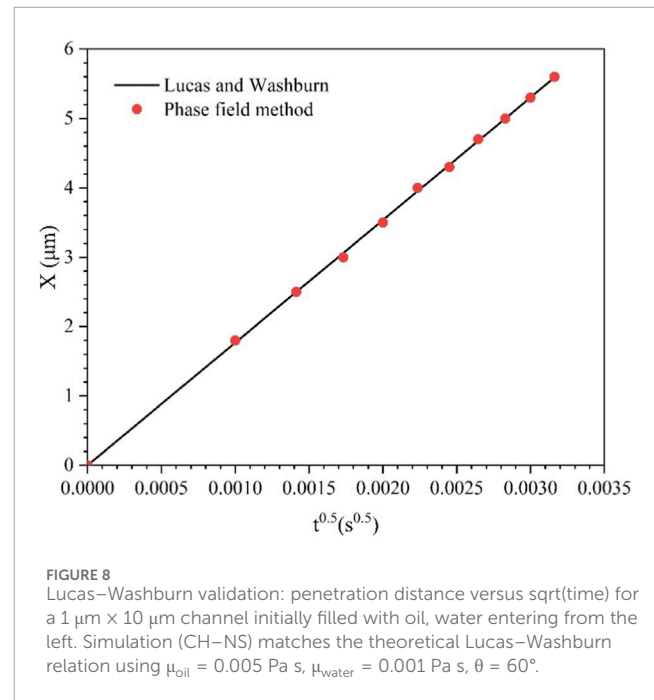
### 3.3 Model validation

To validate the applicability of the phase field method in simulating oil-water two-phase flow, a simulation was conducted using this approach on a horizontal channel measuring  $1 \mu\text{m} \times 10 \mu\text{m}$ , following the validation methodology proposed by Wang et al. (Wang et al., 2024). The channel was initially filled with oil, while the water phase entered from the left side. The model disregarded the effects of gravity and inertial forces. The simulation results were then compared with the theoretical equations put forth (Equation 13) by Lucas (Lucas, 1918) and Washburn (Washburn, 1921).

$$x(t) = \sqrt{\frac{r\sigma \cos \theta}{2\mu}} t \quad (13)$$

Where  $\mu$  is the viscosity of the wetting liquid,  $\text{Pa}\cdot\text{s}$ ;  $\theta$  is the contact angle,  $^\circ$ ;  $r$  is the tube radius, m;  $\sigma$  is the surface tension of the wetting liquid,  $\text{N/m}$ .

The comparative results are illustrated in Figure 8, where the viscosities of oil and water were set at 0.005 Pa s and 0.001 Pa s, respectively, and the contact angle was established at  $60^\circ$ . The simulation results align closely with the calculated outcomes of the theoretical equations, thereby verifying that the phase field method can accurately model the migration behavior of oil and water at pore-throat scales.

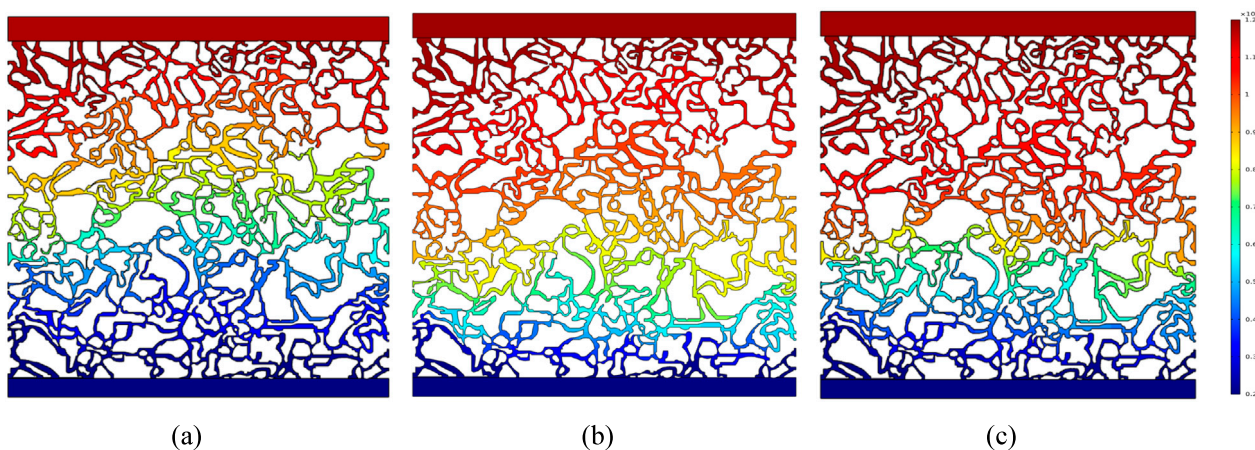


### 3.4 Simulation results analysis

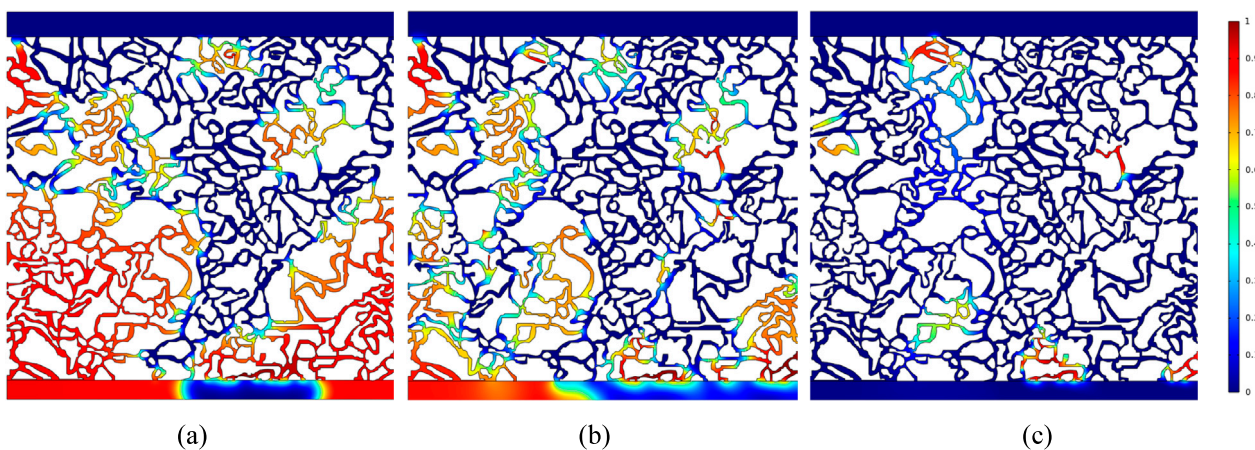
Based on the established simulation plan, micro-simulations of advanced fracturing-flooding water injection at varying scales have been completed, resulting in pressure fields of different scales of advanced injection, as depicted in Figure 9. As the scale of pre-injection increases, the pressure at the inlet gradually rises, which is consistent with the findings from the core experiments.

Figure 10 illustrates the oil saturation fields for different scales of advanced fracturing-flooding water injection. Due to the relatively small pressure gradient at both ends of conventional water injection, in Figure 10a, the injected water primarily displaces crude oil along the main flow path, mainly mobilizing the oil within larger pore throats, while the crude oil trapped in the smaller throats remains largely inaccessible, resulting in a high residual oil saturation and a low overall recovery rate. However, as the scale of advanced fracturing-flooding water injection increases, the pressure gradient at both the injection and production ends progressively intensifies. In Figures 10b,c, the crude oil in smaller pore throats becomes mobilized, leading to a gradual decrease in residual oil saturation, an expanded range of water displacement, and an overall enhancement in recovery efficiency.

Figure 11 depicts the streamline fields of pore throats at varying scales of advanced fracturing-flooding water injection. In contrast to the oil saturation fields, it is evident that during conventional water injection, the main streamlines are primarily distributed along the larger pore throats, forming dominant pathways, while the number of streamlines within the smaller throats is nearly nonexistent. Consequently, with a relatively low pressure gradient, the utilization predominantly occurs within the larger throats, rendering the smaller throats largely ineffective. However, as the scale of advanced fracturing-flooding water injection increases, the pressure gradient is gradually amplified, resulting in an increase in the number of streamlines within the smaller pores. The enhanced



**FIGURE 9**  
Pressure field simulation results of different pre-injection scales (Red indicates higher pressure; blue indicates lower pressure). (a) Conventional injection. (b) 0.3 PV of advanced injection. (c) 0.6 PV of advanced injection.



**FIGURE 10**  
Oil saturation field simulation results of different pre-injection scales (Red indicates kerosene saturation; blue indicates water saturation). (a) Conventional injection. (b) 0.3 PV of advanced injection. (c) 0.6 PV of advanced injection.

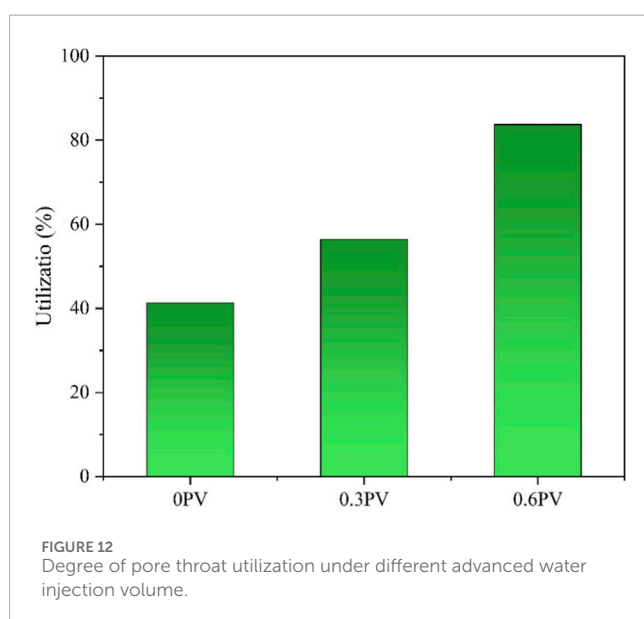
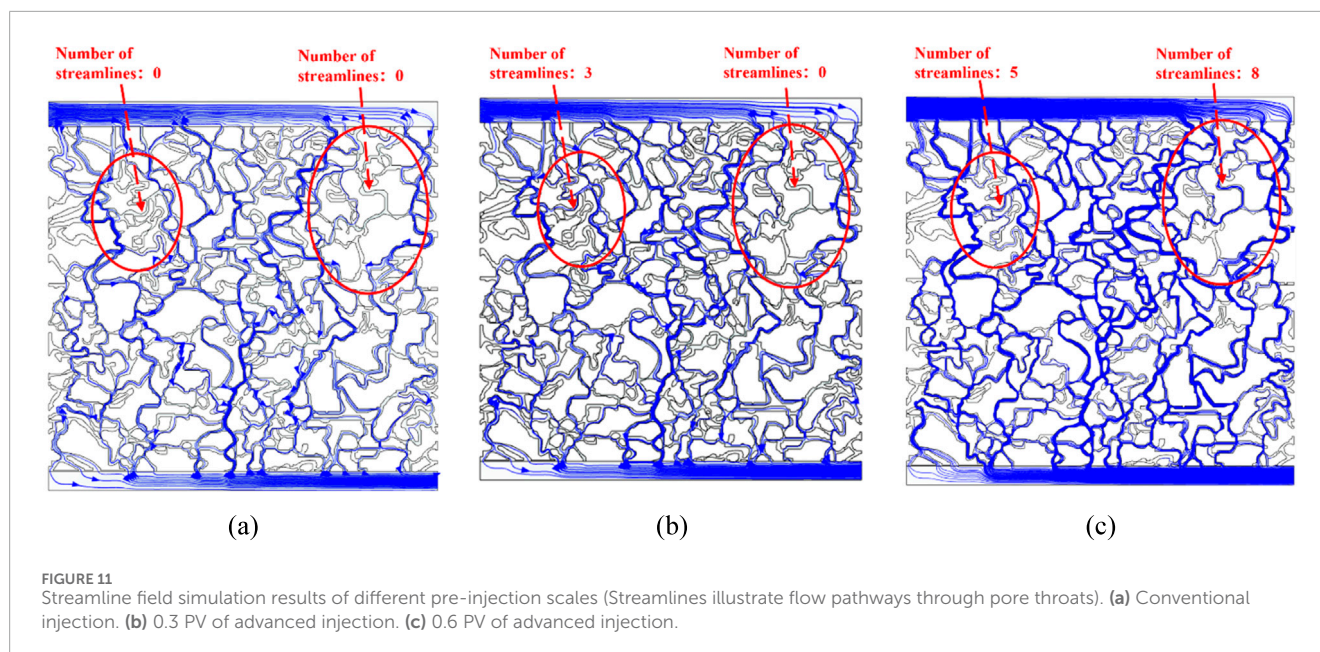
pressure differentials enable both large and small pore throats to be mobilized, leading to an overall increase in the degree of utilization (Figure 12).

## 4 Discussion

AFWI pre-injection at near-fracture pressures, followed by continuous waterflooding, elevates  $\Delta p$  and deepens front penetration. We interpret waterflood performance using three metrics: initial displacement pressure differential ( $\Delta p$ ), front advancement distance, and pore-size-resolved recovery from NMR. Under conventional waterflood (no pre-injection),  $\Delta p$  is limited and the front advances primarily along larger pathways, leaving kerosene stranded in small throats. AFWI increases  $\Delta p$  (6.34  $\rightarrow$  7.56  $\rightarrow$  8.45 MPa with  $V_{pre} = 0 \rightarrow 0.3 \rightarrow 0.6$  PV), extends the front (1.5 cm and 2.6 cm for  $V_{pre} = 0.3$  and 0.6 PV), and raises ultimate

recovery (35.5%  $\rightarrow$  40.5%  $\rightarrow$  43.5%). These trends are consistent with capillary-controlled displacement at low Ca, where elevated pressure gradients are required to overcome local entry pressures in tight constrictions.

The steeper gradient desaturates constricted throats and opens pathways, evidenced by denser small-throat streamlines in simulations and reduced LF-NMR oil signals in small and medium pore bins. To mechanistically resolve the core observations, we performed pore-throat phase-field FE simulations coupled to LF-NMR flooding via harmonized boundary conditions. For  $V_{pre} = 0, 0.3,$  and 0.6 PV, the inlet–outlet  $\Delta p$  recorded during pre-injection (producers closed) and subsequent waterflooding (producers open) specified the simulation inputs. The inlet was prescribed as a velocity boundary to reproduce the  $\Delta p$  trajectory, while the outlet matched the back-pressure settings, yielding pressure fields that captured gradient steepening without spurious inertia. Fluid properties and wettability (density, viscosity, interfacial tension, contact angle)



were matched to produce capillary numbers representative of tight rocks. Using SEM-derived geometries that preserve throat-size statistics, we computed streamline density, local velocities, and oil-saturation changes, delineating small-throat domains via curvature/contraction metrics. Increasing  $V_{pre}$  raised streamline counts and lowered residual oil in these domains, mirroring LF-NMR observations in small and medium pore bins. Overall, larger pre-injection volumes steepened the gradient, activated quiescent pathways, and reduced residual saturation, consistent with recovery gains.

Consistent reports across tight sandstones and shales (Farouk et al., 2025a; Farouk et al. 2025b; Farouk et al. 2024) show that pressure-managed modes improve sweep and mobilize oil from

small throats, with gains contingent on lithology, pore architecture, and wettability. Differences in mineralogy, cement, and throat-size distributions will tune optimal AFWI parameters; formations rich in small throats may require higher, tightly controlled pre-injection or wettability adjustment. Limitations include three cores and 2D SEM-derived simulations that omit full 3D connectivity and spatial wettability variability. Future work should expand core sets, employ micro-CT reconstructions, probe sensitivities to wettability, interfacial tension, and rate, and couple microfracture generation with pore-scale flow; field pilots calibrated by NMR pore-size distributions will refine operational envelopes.

## 5 Conclusion

This study investigates the utilization characteristics of microscopic pore throats during advanced fracturing-flooding water injection through core displacement experiments and micro-simulations at various scales. The following conclusions have been drawn:

1. In comparison to conventional waterflood development, advanced fracturing-flooding water injection enhances the injection end pressure prior to the development phase, elevating the pressure gradient at both the injection and production ends and facilitating the early utilization of crude oil at the inlet.
2. Advanced fracturing-flooding water injection increases the utilization of crude oil within medium to small pore throats, and as the scale of advanced fracturing-flooding water injection expands, the elevation in pressure, the propagation distance of pressure, and the advancement distance of the water displacement front also increase correspondingly.
3. With the escalation of the pressure gradient, the number of streamlines in medium to small pore throats progressively rises. Under low pressure gradients, utilization predominantly

occurs in larger pore throats, making it challenging to access smaller ones. However, as the pressure gradient intensifies, significant pressure differentials enable both large and small pores to be mobilized, resulting in a high degree of utilization.

## Data availability statement

The original contributions presented in the study are included in the article/supplementary material, further inquiries can be directed to the corresponding author.

## Author contributions

JS: Writing – review and editing, Conceptualization, Funding acquisition, Project administration, Writing – original draft, Methodology. QZ: Writing – original draft, Writing – review and editing, Methodology, Conceptualization. JL: Writing – review and editing, Methodology, Writing – original draft, Conceptualization. MZ: Formal Analysis, Writing – review and editing. LS: Writing – review and editing. DW: Writing – review and editing.

## Funding

The author(s) declared that financial support was received for this work and/or its publication. This research was supported by the National Natural Science Foundation of China project titled “Rearrangement Mechanisms of Oil-Gas Systems and Hydrodynamic Property Characterization in Organic-Rich Shale Nanopores” (52174038), as well as by the National Key Technology Research and Development Program titled “Demonstration of Enhanced Oil Recovery Technologies in Dense Sandstone Reservoirs” (2025ZD1405402).

## References

- Cao, H., Zhang, Z. Q., Li, S. Y., Zhou, D. W., Yu, C. L., and Sun, Q. (2024). Fracturing initiation and breakdown pressures in fracturing-flooding sandstone reservoirs. *Rock Mech. Rock Eng.* doi:10.1007/s00603-024-04186-w
- Chelsea, N., Saurabh, T., and Zoya, H. (2020). Simultaneous assessment of wettability and water saturation using 2D NMR measurements. *Fuel* 270, 117431. doi:10.1016/j.fuel.2020.117431
- Farouk, S., Mohammad, A. S., Souvik, S., Fayed, A., Al-Kahtany, K., and Reda, M. M. (2024). Evaluation of the Lower Cretaceous alam El Bueib sandstone reservoirs in Shushan Basin, Egypt – implications for tight hydrocarbon Reservoir potential. *J. Afr. Earth Sci.* 218 (October), 105386. doi:10.1016/j.jafrearsci.2024.105386
- Farouk, S., Abdelrahman, Q., Souvik, S., Ahmad, F., El-Kahtany, K., Collier, R., et al. (2025a). Characterization of the gas-bearing tight Paleozoic sandstone reservoirs of the Risha field, Jordan: inferences on reservoir quality and productivity. *Arabian J. Sci. Eng.* 50 (1), 215–235. doi:10.1007/s13369-024-09000-x
- Farouk, S., Souvik, S., Sayantan, G., Partha, P. M., Fathy, M., and Sarhan, M. A. (2025b). *In-Situ* stress State of the Shushan Basin, Western desert, Egypt: implications for developing tight Cretaceous and Paleozoic reservoirs. *Arabian J. Sci. Eng.* 31, petgeo2025-004. doi:10.1007/s13369-025-10766-x
- Feng, C. J., Yang, H., Pu, R. H., Wang, Y., Wang, D., Liang, X., et al. (2017). Lithology and oil-bearing properties of tight sandstone reservoirs: Chang 7 member of Upper Triassic Yanchang Formation, Southwestern Ordos Basin, China. *Geosciences J.* 21 (2), 201–211. doi:10.1007/s12303-016-0048-3
- Feng, M., Sun, L., and Sun, L. (2025). Characterization of pore structure and simulation of pore-scale flow in tight sandstone reservoirs. *Fluid Dyn. Mater. Process.* 21 (3), 573–587. doi:10.32604/fdmp.2024.056421
- Gao, Y. B., Zhu, W. Y., Bu, W. G., Yue, M., and Kong, D. B. (2024). A fast and reliable semi-analytical method for assessing energy replenishment from fracturing-flooding in low-permeability and tight oil reservoirs. *Phys. Fluids* 36 (9), 96605. doi:10.1063/5.0225841
- Hou, P., Liang, X., Gao, F., Dong, J. B., He, J., and Xue, Y. (2021). Quantitative visualization and characteristics of gas flow in 3D pore-fracture system of tight rock based on lattice Boltzmann simulation. *J. Nat. Gas Sci. Eng.* 89 (May), 103867. doi:10.1016/j.jngse.2021.103867
- Jamal, A. H., Riyadh, I. A., Zaher, A. J., Khalid, A. A., and Jongwon, J. (2022). Fines effect on gas flow in sandy sediments using  $\mu$ CT and pore networks. *J. Nat. Gas Sci. Eng.* 108, 104834. doi:10.1016/j.jngse.2022.104834
- Jia, Z. H., Cao, R. Y., Pu, B. B., Dehghanpour, H., Cheng, L., Zhang, Q., et al. (2025). Pore-Scale binary diffusion behavior of hydrogen-cushion gas in saline aquifers for underground hydrogen storage: optimization of cushion gas type. *Fuel* 381 (February), 133481. doi:10.1016/j.fuel.2024.133481
- Jin, G. W., Xie, R. H., Xiao, L. Z., Wu, B., Xu, C., Wang, X., et al. (2021). Quantitative characterization of bound and movable fluid microdistribution in porous rocks using nuclear magnetic resonance. *J. Petroleum Sci. & Eng.* 196 (January), 107677. doi:10.1016/j.petrol.2020.107677

## Conflict of interest

Authors JS, JL, LS, and DW were employed by Exploration & Development Research Institute of Petrol China Changqing Oilfield Company.

The remaining author(s) declared that this work was conducted in the absence of any commercial or financial relationships that could be construed as a potential conflict of interest.

The reviewer BW declared a shared affiliation with the authors QZ, MZ to the handling editor at time of review.

## Generative AI statement

The author(s) declared that generative AI was not used in the creation of this manuscript.

Any alternative text (alt text) provided alongside figures in this article has been generated by Frontiers with the support of artificial intelligence and reasonable efforts have been made to ensure accuracy, including review by the authors wherever possible. If you identify any issues, please contact us.

## Publisher's note

All claims expressed in this article are solely those of the authors and do not necessarily represent those of their affiliated organizations, or those of the publisher, the editors and the reviewers. Any product that may be evaluated in this article, or claim that may be made by its manufacturer, is not guaranteed or endorsed by the publisher.

- Krakowska, P. I., and Puskarczyk, E. (2015). Tight reservoir properties derived by nuclear magnetic resonance, Mercury porosimetry and computed microtomography laboratory techniques. Case study of Palaeozoic clastic rocks. *Acta Geophys.* 63 (3), 789–814. doi:10.1515/ageo-2015-0013
- Lang, D. J., Lun, Z. M., Lyu, C. Y., Wang, H. T., Zhao, Q. M., and Han, S. (2021). Nuclear magnetic resonance experimental study of CO<sub>2</sub> injection to enhance shale oil recovery. *Petroleum Explor. Dev.* 48 (3), 702–712. doi:10.1016/S1876-3804(21)60056-3
- Li, C., Chen, G. J., Li, X. T., Zhou, Q. S., and Sun, Z. T. (2022a). The occurrence of tight oil in the Chang 8 lacustrine sandstone of the huaqing area, ordos Basin, China: insights into the content of adsorbed oil and its controlling factors. *J. Nat. Gas Geoscience* 7 (1), 27–37. doi:10.1016/j.jnggs.2021.11.001
- Li, S., Yang, S. L., Gao, X. Y., Wang, M. B., and Yu, J. Y. (2022b). Experimental study on liquid production law, oil recovery mechanism, and influencing factors of water Huff-n-Puff in the tight sedimentary tuff oil reservoir. *J. Petroleum Sci. Eng.* 208 (January), 109721. doi:10.1016/j.petrol.2021.109721
- Li, N. Y., Zhu, S. J., Li, Y., Zhao, J., Long, B., Chen, F., et al. (2024). Fracturing-flooding technology for low permeability reservoirs: a review. *Petroleum* 10 (2), 202–215. doi:10.1016/j.petlm.2023.11.004
- Li, P. Y., Song, Y. L., Jiang, J. T., Song, Z., Han, X., Wang, X., et al. (2025). Pore-scale simulation of oil-water flow in shale media after fracture hits: an integrated approach using U-Net and lattice boltzmann method. *Fuel* 402 (December), 136038. doi:10.1016/j.fuel.2025.136038
- Lin, W., Xiong, S. C., Liu, Y., He, Y., Chu, S. S., and Liu, S. Y. (2021). Spontaneous imbibition in tight porous media with different wettability: pore-scale simulation. *Phys. Fluids* 33 (3), 032013. doi:10.1063/5.0042606
- Liu, J. R., Li, H. Y., Tan, Q. Z., Liu, S. Y., Zhao, H. L., and Wang, Z. Q. (2022). Quantitative study of CO<sub>2</sub> Huff-n-Puff enhanced oil recovery in tight formation using online NMR technology. *J. Petroleum Sci. & Eng.* 216 (September), 110688. doi:10.1016/j.petrol.2022.110688
- Lu, X., Abdolreza, K., and Evangelos, T. (2020). Transport parameters of macroscopic continuum model determined from discrete pore network simulations of drying porous media: throat-node vs. throat-pore configurations. *Chem. Eng. Sci.* 223, 115723. doi:10.1016/j.ces.2020.115723
- Lucas, R. (1918). Ueber Das Zeitgesetz Des Kapillaren Aufstiegs von Flüssigkeiten. *Kolloid Z.* 23 (1), 15–22. doi:10.1007/BF01461107
- Mahmoud, E., Mohamed, M., Ammar, E., Muhammad, S. K., and Karem, A. (2020). A new method to evaluate reaction kinetics of acids with carbonate rocks using NMR diffusion measurements. *Energy Fuels* 34, 787–797. doi:10.1021/acs.energyfuels.9b03784
- Mohnke, O., Stiebler, M., and Klitzsch, N. (2014). Joint numerical microscale simulations of multiphase flow and NMR relaxation behavior in porous media using Lattice Boltzmann methods. *Water Resour. Res.* 50, 7378–7393. doi:10.1002/2013wr014684
- Oluwasanmi, O., Pastor, A., Charles, O., Christopher, N., and Seyi, O. (2021). Optimizing productivity in oil rims: simulation studies on water and gas injection patterns. *Arabian J. Geosciences* 14 (7), 579. doi:10.1007/s12517-021-06945-3
- Qi, D. C., Liu, W. Q., Guo, C. B., Ma, T., Wang, Z., Song, C., et al. (2024). Experimental investigation on CO<sub>2</sub> flooding for enhanced light oil recovery in low-permeability sandstones under multiple controlling factors by online nuclear magnetic resonance testing. *Phys. Fluids* 36 (12), 126616. doi:10.1063/5.0243277
- Ren, J. T., Xiao, W. L., Cheng, Q. R., Song, P., Bai, X., Xie, Q., et al. (2025). Experimental study on Water/CO<sub>2</sub> flow of tight oil using HTHP microscopic visualization and NMR technology. *Geoenergy Sci. Eng.* 250 (July), 213834. doi:10.1016/j.geoen.2025.213834
- Shi, L. Z., Wang, Z. Z., Zhang, G., Zhang, Y. S., and Xing, E. Y. (2015). Distribution and formation of tight oil in Qijia area, Songliao Basin, NE China. *Petroleum Explor. Dev.* 42 (1), 48–55. doi:10.1016/S1876-3804(15)60005-2
- Song, Z. J., Song, Y. L., Li, Y. Z., Bai, B. J., Song, K. P., and Hou, J. R. (2020). A critical review of CO<sub>2</sub> enhanced oil recovery in tight oil reservoirs of North America and China. *Fuel* 276 (September), 118006. doi:10.1016/j.fuel.2020.118006
- Sun, Z. H., Li, M. H., Yuan, S., Hou, X., Bai, H., Zhou, F., et al. (2024). The flooding mechanism and oil recovery of nanoemulsion on the Fractured/non-fractured tight sandstone based on online LF-NMR experiments. *Energy* 291 (March), 130226. doi:10.1016/j.energy.2023.130226
- Tan, M. J., Wang, K., Zou, Y. L., Wang, S. Y., Fang, Y. Y., and Cheng, X. Z. (2019). Nuclear magnetic resonance simulations of nano-scale cores and microscopic mechanisms of oil shale. *Fuel* 256 (November), 115843. doi:10.1016/j.fuel.2019.115843
- Wang, J., Liu, H. Q., Qian, G. B., Peng, Y. C., and Gao, Y. (2019). Investigations on spontaneous imbibition and the influencing factors in tight oil reservoirs. *Fuel* 236, 755–768. doi:10.1016/j.fuel.2018.09.053
- Wang, W., Li, Y. H., and Chen, X. L. (2021). Microscope dynamic characterization of oil charging in tight sandstone using a physical simulation experiment. *J. Petroleum Sci. & Eng.* 200 (May), 108379. doi:10.1016/j.petrol.2021.108379
- Wang, B. Y., Cao, R. Y., Pi, Z. Y., Cheng, L. S., Jia, Z. H., and Hu, J. P. (2024). Displacement-imbibition coupling mechanisms between matrix and complex fracture during injecting-shut in-Production process using pore-scale simulation and NMR experiment. *Geoenergy Sci. Eng.* 242 (November), 213254. doi:10.1016/j.geoen.2024.213254
- Wang, B. Y., Cao, R. Y., Zheng, X. Y., Cheng, L. S., Hu, J. P., Jia, Z. H., et al. (2025). Real-time NMR experimental study of displacement-imbibition coupling in tight/shale oil reservoirs: lithological variations, influencing factors, and key insights. *Petroleum Sci.*, S1995822625003048. doi:10.1016/j.petsci.2025.08.028
- Washburn, E. W. (1921). The dynamics of capillary flow. *Phys. Rev.* 17 (3), 273–283. doi:10.1103/PhysRev.17.273
- Wei, J. G., Zhang, A., Li, J. T., Liu, X., Wang, A., Yang, Y., et al. (2023). Study on oil seepage mechanisms in lamellar shale by using the lattice Boltzmann method. *Fuel* 351 (November), 128939. doi:10.1016/j.fuel.2023.128939
- Xu, Z. P., Lin, M., Ji, L. L., Jiang, W. B., Cao, G. H., and Xu, L. G. (2023). Multiscale pore-fracture hybrid pore network modeling for drainage in tight carbonate. *Adv. Water Resour.* 174 (April), 104420. doi:10.1016/j.advwatres.2023.104420
- Xue, L., Zhang, J., Chen, G., Wang, X., Huang, X., Li, X., et al. (2025). Enhance oil recovery by carbonized water flooding in tight oil reservoirs. *Geoenergy Sci. Eng.* 244 (January), 213430. doi:10.1016/j.geoen.2024.213430
- Yan, B., Liu, H. Y., and Peng, X. Y. (2024). Scenario analysis to evaluate the economic benefits of tight oil resource development in China. *Energy Strategy Rev.* 51 (January), 101318. doi:10.1016/j.esr.2024.101318
- Yang, H., Liang, X. W., Niu, X. B., Feng, S. B., and You, Y. (2017). Geological conditions for Continental tight oil Formation and the main controlling factors for the enrichment: a case of Chang 7 member, Triassic Yanchang formation, ordos Basin, NW China. *Petroleum Explor. Dev.* 44 (1), 11–19. doi:10.1016/S1876-3804(17)30003-4
- Yang, J. R., Liu, X. Y., and Xu, W. L. (2022a). Reservoir forming dynamics of differential accumulation of tight oil in the Yanchang formation chang 8 member in the Longdong area, ordos Basin, central China. *Front. Earth Sci.* 9, 788826. doi:10.3389/feart.2021.788826
- Yang, Y. B., Xiao, W. L., Bernabe, Y., Xie, Q., Wang, J., He, Y., et al. (2022b). Effect of pore structure and injection pressure on waterflooding in tight oil sandstone cores using NMR technique and pore network simulation. *J. Petroleum Sci. & Eng.* 217 (October), 110886. doi:10.1016/j.petrol.2022.110886
- Yang, M. Y., Huang, S. J., Zhao, F. L., Sun, H. Y., and Chen, X. Y. (2024). Experimental investigation of CO<sub>2</sub> Huff-n-Puff in tight oil reservoirs: effects of the fracture on the dynamic transport characteristics based on the nuclear magnetic resonance and fractal theory. *Energy* 294 (May), 130781. doi:10.1016/j.energy.2024.130781
- Yao, L. L., Lei, Q. H., Yang, Z. M., He, Y., Li, H., Zhao, G., et al. (2023). Online nuclear magnetic resonance analysis of the effect of stress changes on the porosity and permeability of shale oil reservoirs. *Energies* 16 (3), 1139. doi:10.3390/en16031139
- Yuan, Y. J., Reza, R., Zhou, M. F., and Stefan, I. (2023). A comprehensive review on shale studies with emphasis on Nuclear magnetic resonance (NMR) technique. *Gas Sci. Eng.* 120 (December), 205163. doi:10.1016/j.jgsce.2023.205163
- Yue, P. T., Zhou, C. F., James, J. F., Carl, F., Ollivier, G., and Howard, H. H. (2006). Phase-field simulations of interfacial dynamics in viscoelastic fluids using finite elements with adaptive meshing. *J. Comput. Phys.* 219 (1), 47–67. doi:10.1016/j.jcp.2006.03.016
- Zhang, X. S., Wang, H. J., Ma, F., Sun, X. C., Zhang, Y., and Song, Z. H. (2016). Classification and characteristics of tight oil plays. *Petroleum Sci.* 13 (1), 18–33. doi:10.1007/s12182-015-0075-0
- Zhang, Q. P., Yang, C., Gu, Y., Tian, Y., Liu, H., Xiao, W., et al. (2025). Microscopic pore-throat structure and fluid mobility of tight sandstone reservoirs in multi-provenance systems, Triassic Yanchang formation, Jiyuan Area, ordos Basin. *Energy Geosci.* 6 (2), 100407. doi:10.1016/j.engeos.2025.100407
- Zhao, Z. T., Jiang, S., Lei, T., Wang, J. W., and Zhang, Y. F. (2025). Optimization of key parameters of fracturing flooding development in offshore reservoirs with low permeability based on numerical modeling approach. *J. Mar. Sci. Eng.* 13 (2), 282. doi:10.3390/jmse13020282
- Zhou, C. F., Yue, P. T., James, J. F., Carl F. O. G., and Howard, H. H. (2010). 3D phase-field simulations of interfacial dynamics in newtonian and viscoelastic fluids. *J. Comput. Phys.* 229 (2), 498–511. doi:10.1016/j.jcp.2009.09.039
- Zhou, H. D., Zhang, Q. S., Dai, C. L., Li, Y., Lv, W., Wu, Y., et al. (2019). Experimental investigation of spontaneous imbibition process of Nanofluid in ultralow permeable Reservoir with nuclear magnetic resonance. *Chem. Eng. Sci.* 201 (June), 212–221. doi:10.1016/j.ces.2019.02.036